Improvement in the GERB short wave flux estimations over snow covered surfaces

C. Bertrand *, L. Gonzalez, A. Ipe, N. Clerbaux, S. Dewitte

Royal Meteorological Institute of Belgium, 3 Avenue circulaire, B-1180 Brussels, Belgium

Abstract

Because space-borne radiometers do not measure the Earth's outgoing fluxes directly, angular distribution models (ADMs) are required to relate actual radiance measurement to flux at given solar angle, satellite-viewing geometries, surface, and atmospheric conditions. The conversion of one footprint broad-band radiance into the corresponding flux requires therefore one to first characterize each footprint in terms of surface type and cloud cover properties to properly select the adequate ADM.

A snow (and sea-ice) retrieval technique based on spectral measurements from the Spinning Enhanced Visible and Infrared Imager (SEVIRI) on board Meteosat 8 is presented. It has been developed to improve the scene identification and thus the ADM selection in the near-real time processing of the Geostationary Earth Radiation Budget (GERB) data at the Royal Meteorological Institute of Belgium. The improvement in the GERB short wave flux estimations over snow covered scene types resulting from angular conversion using dedicated snow ADMs (e.g., empirical snow ADMs and/or pre-computed theoretical snow ADM) instead of empirical snow-free ADMs is discussed.

© 2006 COSPAR. Published by Elsevier Ltd. All rights reserved.

Keywords: Remote sensing; Snow cover; Short wave flux; Radiance-to-flux conversion; Angular distribution model

1. Introduction

Snow cover is among the most important of the Earth's surface characteristics that influence surface radiation, energy, and hydrological budgets (e.g., Foster and Chang, 1993). Compared to other land covers, its areal extent dramatically varies on very short time scales (hours to months). Fortunately, satellites are well suited to the detection of snow cover as snow exhibits a specific spectral reflectance pattern with high values in the visible (VIS) and low reflectance in the short wave infrared (SWIR) and middle infrared (MIR) part of the spectrum (Wiscombe and Warren, 1980), which is different from the spectral reflectance of many other natural surfaces and clouds. This specific spectral feature of snow (which is fairly constant over a wide range of land surfaces and illumination conditions) is widely exploited in automated and semi-automated snow detection techniques based on satellite observations in the VIS, SWIR, MIR, and IR (e.g., Gesell, 1989; Key and Barry, 1989; Hall et al., 1995; Romanov et al., 2000).

Snow, like all natural surfaces, is an anisotropic reflector (e.g., Dirmhirn and Eaton, 1975; Steffen, 1987; Nolin and Liang, 2000). The reflectance from snow is greatest in the forward direction and is largely specular. Note that while freshly fallen snow can be nearly a Lambertian reflecting surface, as snow metamorphoses, the specular component characteristic of forward scattering increases (Dirmhirn and Eaton, 1975; Steffen, 1987). Because the energy reflected from a snow surface is unevenly distributed among reflection angles, knowledge of the actual angular distribution of this reflected energy is needed to correctly account for anisotropic scattering effects when performing the radiance-to-flux conversion.

In this contribution, we present a snow (and sea-ice) mapping technique using observations from the Spinning Enhanced Visible and Infrared Imager (SEVIRI) on board Meteosat 8 (MS-8) (Schmetz et al., 2002) to be incorporated into the near-real time processing of the data provided by the Geostationary Earth Radiation Budget (GERB) instrument (Harries et al., 2005), the broad-band (BB) radiometer on board MS-8. In addition we investigate the impact of the use of snow angular distribution models (ADMs) when performing the radiance to flux conversion over snow covered footprints on the GERB short wave (SW) flux estimations instead of snow-free ADMs as currently done. Prior to describing the snow (and sea-ice) mapping algorithm, we first start by briefly describing the method implemented at the Royal Meteorological Institute of Belgium (RMIB) to estimate the top-of-atmosphere (TOA) reflected GERB SW fluxes from the combined use of SEVIRI and GERB data.

2. Derivation of the TOA reflected GERB SW fluxes

Accurate estimation of the unfiltered reflected solar radiances requires that the variations of the instrument's sensitivity with wavelength are removed from the filtered directional SW radiance measurements, L_{SW}^f. Basically, SEVIRI narrow-band (NB) measurements are used to retrieve information about the spectral distribution of the observed radiation. The unfiltered BB SW radiances, L_{SW}^{uf}, are estimated by multiplying the filtered GERB BB SW measurements, L_{GERB}^f, by the corresponding SEVIRI BB unfilter factor, $\alpha (= L_{SEVIRI_{BB}}^{uf}/L_{SEVIRI_{BB}}^f)$:

$$L_{GERB}^{uf} = \left(\frac{L_{SEVIRI_{BB}}^{uf}}{L_{SEVIRI_{BB}}^f}\right) \cdot L_{GERB}^f$$
$$= L_{SEVIRI_{BB}}^{uf} \cdot \left(\frac{L_{GERB}^f}{L_{SEVIRI_{BB}}^f}\right) = L_{SEVIRI_{BB}}^{uf} \cdot C_L, \quad (1)$$

where L_{GERB}^f is the filtered GERB BB SW radiance measurement. $L_{SEVIRI_{BB}}^f$ and $L_{SEVIRI_{BB}}^{uf}$ are the estimates of the GERB filtered and unfiltered BB SW radiances measurements computed from the SEVIRI spectral radiances only. C_L is the pixel dependent correction factor (i.e., $L_{GERB}^f/L_{SEVIRI_{BB}}^f$) at the nominal GERB spatial resolution (i.e., 50 km at the sub-satellite point).

The unfiltered SEVIRI BB SW radiance, $L_{SEVIRI_{BB}}^{uf}$ is computed from the SEVIRI imager through narrow-band to broad-band (NB-to-BB) conversion and convolution with the GERB point spread function (PSF). The spectral conversion (NB-to-BB) is performed by the way of polynomial regressions on the SEVIRI NB reflectances. NB-to-BB regressions were derived empirically for five surface types (i.e., ocean, dark vegetation, bright vegetation, dark desert, and bright desert surfaces) independently of the cloud conditions from a database of co-angular unfiltered BB SW radiances measured by the Clouds and the Earth's Radiant Energy System (CERES) instruments (Wielicki et al., 1996)

and spectral SEVIRI data. The CERES ES8 Edition-2 data for the FM2 (on Terra) and FM3 (on Aqua) instruments for the months of March, April and July 2004, were considered (Clerbaux et al., 2005). For each surface type the regressions have the following form:

$$\rho_{SEVIRI_{BB}}^{uf} = c_0 + c_1\rho_{0.6} + c_2\rho_{0.6}^2 + c_3\rho_{0.8} + c_4\rho_{1.6}$$
$$+ c_5\theta_s + c_6\gamma, \quad (2)$$

where θ_s is the solar zenith angle, and γ is the sun glint angle $(\cos\gamma = \mu_s\mu_v + \sqrt{(1-\mu_s)^2}\sqrt{(1-\mu_v)^2}\cos(\phi))$ with μ_s and μ_v the cosines of the solar and viewing zenith angles, respectively. ϕ is the relative azimuth angle. c_i $(i = 1,\ldots,6)$ are the regression coefficients which vary according to the surface type. $\rho_{0.6}$, $\rho_{0.8}$, and $\rho_{1.6}$ are the spectral reflectances of the SEVIRI instruments in its spectral bands centered at 0.6, 0.8, and 1.6 μm, respectively. Note that the reflectances in Eq. (2) are obtained by normalizing the corresponding radiances by the incoming solar radiance, L_{sol}, the cosines of the solar zenith angle, $\cos\theta_s$, and the Earth–Sun distance, d $(\rho = L/(L_{sol}\cos\theta_s/d^2))$. Due to the very sparse distribution of snow covered pixels within the SEVIRI field-of-view (FOV), the regression coefficients, c_i, for the NB-to-BB conversion over snow surface in Eq. (2) were derived theoretically from a database of simulated spectral radiances.

The estimation of the filtered GERB BB SW radiance from the SEVIRI NB measurements, $L_{SEVIRI_{BB}}^f$, is obtained through NB-to-BB equations exhibiting the same analytical form as the one given in Eq. (2):

$$\rho_{SEVIRI_{BB}}^f = c_0' + c_1'\rho_{0.6} + c_2'\rho_{0.6}^2 + c_3'\rho_{0.8} + c_4'\rho_{1.6}$$
$$+ c_5'\theta_s + c_6'\gamma. \quad (3)$$

Similarly to Eq. (2), the regression coefficients c_i' in Eq. (3) are surface types dependent but independent of the cloud conditions. However, because the CERES and GERB spectral responses differ, it was not possible to derive the regression coefficients c_i' in Eq. (3) empirically (e.g., from a database of co-angular filtered BB SW CERES radiances and SEVIRI spectral data). Instead, $L_{SEVIRI_{BB}}^f$ can be estimated by:

$$L_{SEVIRI_{BB}}^f = L_{SEVIRI_{BB}}^{uf}/\alpha_{rtm}, \quad (4)$$

where α_{rtm} is a theoretical unfilter factor (L_{rtm}^{uf}/L_{rtm}^f) calculated from a database of theoretical spectral radiances $(L_{rtm}^{uf}$ and L_{rtm}^f being theoretical estimations of the unfiltered and filtered GERB BB SW radiances, respectively). To obtain consistent estimations of $L_{SEVIRI_{BB}}^f$, the regression parameters c_i' in Eq. (3) were fitted on the theoretical radiative transfer model simulations as follows:

$$\frac{c_0' + c_1'\rho_{(0.6,rtm)} + c_2'\rho_{(0.6,rtm)}^2 + c_3'\rho_{(0.8,rtm)} + c_4'\rho_{(1.6,rtm)} + c_5'\theta_s + c_6'\gamma}{c_0 + c_1\rho_{(0.6,rtm)} + c_2\rho_{(0.6,rtm)}^2 + c_3\rho_{(0.8,rtm)} + c_4\rho_{(1.6,rtm)} + c_5\theta_s + c_6\gamma}$$

$$= \frac{\rho_{rtm}^f}{\rho_{rtm}^{uf}}, \quad (5)$$

where c_i are the Eq. (2) empirical regression coefficients and $\rho_{j,\text{rtm}}$ ($j = 0.6$, 0.8, and 1.6), $\rho_{\text{rtm}}^{\text{f}}$ and $\rho_{\text{rtm}}^{\text{uf}}$ theoretical radiances.

A large database of theoretical spectral radiances was built by running the Santa Barbara DISORT Atmospheric Radiative Transfer (SBDART) model (Ricchiazzi et al., 1998) for 750 different conditions of the Earth surface, the atmosphere and the cloudiness. The spectral radiances in the database were then convoluted with the GERB and SEVIRI spectral response filters to obtain the filtered BB ($L_{\text{rtm}}^{\text{f}}$) and NB ($L_{j,\text{rtm}}$) SW radiances which were finally expressed in term of reflectance. Note that the c_i coefficients in Eq. (2) for the snow surface were also derived from this spectral radiance database.

Table 1 provides a theoretical estimation of the unfiltering bias (the average of the unfiltering error) and Root Mean Square Error (RMSE) for each surface types as a function of the cloud condition (clear or cloudy). Table 1 indicates that for the different scene types the biases are less than 0.12% and the RMSE less than 1% (clear ocean case discarded). It is worth pointing out that the real error in unfiltering may be underestimated as the values provided in Table 1 do not take into account the difference between the model and the real world. As an example, the failure to include the full range of potential viewing conditions in the theoretical spectral radiances database used to derive the NB-to-BB fits through the use of Lambertian surface reflectance when running the SBDART model (excepted over ocean surface where a Cox and Munk (1954) scheme accounts for ocean surface roughness) could have the effect of producing an artificially low estimate of the RMSE.

Due to the poor performance of our unfiltering scheme over clear ocean surface (see Table 1) a theoretical unfilter factor, $\alpha_{\text{oc-clr}}$, is used in Eq. (1) over clear ocean scene instead of Eqs. (2) and (3):

$$\alpha_{\text{oc-clr}} = a(\theta_s, \theta_v, \phi) + \frac{b(\theta_s, \theta_v, \phi)}{\rho_{0.6}} + \frac{c(\theta_s, \theta_v, \phi)}{\rho_{0.6}^2}, \quad (6)$$

where the regression parameters ($a(\theta_s, \theta_v, \phi)$, $b(\theta_s, \theta_v, \phi)$, and $c(\theta_s, \theta_v, \phi)$) are derived as the best fit over the 301 ocean simulations present in the spectral radiances database. θ_s, θ_v, and ϕ are the solar zenith angle, the viewing zenith angle and the relative azimuth angle, respectively. $\rho_{0.6}$ is the SEVIRI reflectance in its channel centered at 0.6 μm. The unfiltering error associated with the clear ocean regression Eq. (6) is estimated to vary from 0.75% to 1.5% (RMSE) according to the angular geometry. Further information on the GERB unfiltering scheme and the spectral radiances database generation can be found in Clerbaux et al. (2007).

The conversion of a footprint's BB radiance into the corresponding flux requires that each footprint is characterized in terms of surface type and cloud cover properties (i.e., cloud fraction, cloud phase, and cloud optical depth) to properly select the adequate ADM. The cloud information is retrieved from the SEVIRI spectral measurements (see Ipe et al., 2004). The Global Land Cover Map (version v1.2) produced by the International Geosphere Biosphere Program (IGBP; Belward, 1996) is used to select one of the six CERES classes (e.g., ocean, moderate-to-high vegetation, low-to-moderate vegetation, dark desert, bright desert, and permanent snow) for each SEVIRI pixels (see Fig. 1). This is done by merging the IGBP surface types into the CERES surface types. It is worth pointing out that the SEVIRI pixel registration according to the six classes is taken invariant in time and does not take care of the presence of sea-ice and/or fresh snow. Moreover permanent snow is assimilated to bright desert surface when performing the radiance-to-flux conversion. The CERES-TRMM BB SW ADMs (Loeb et al., 2003) are used to perform the SW radiance-to-flux conversion.

$$F_{\text{SW}}(\theta_s) = \pi \cdot \frac{L_{\text{SW}}^{\text{uf}}(\theta_s, \theta_v, \phi)}{R_{\text{SW}}(\theta_s, \theta_v, \phi)}, \quad (7)$$
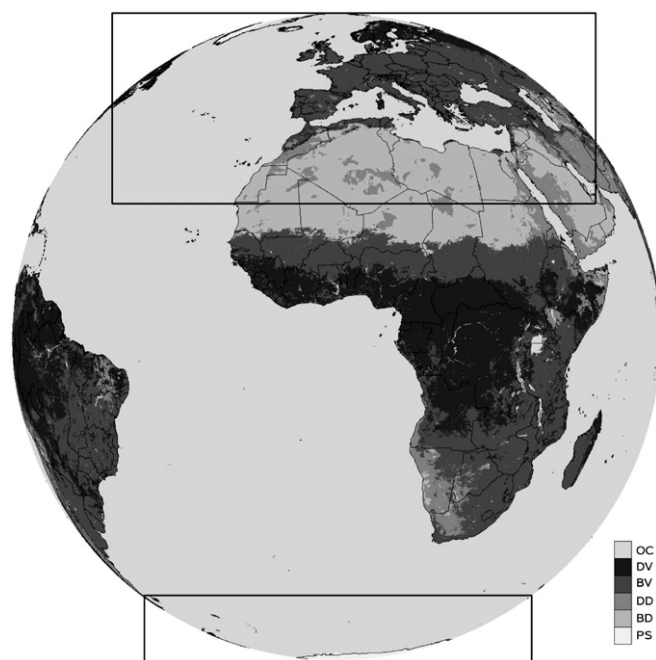

Fig. 1. ADMs surfaces geotypes as seen by SEVIRI imager (OC, ocean; DV, moderate-to-high vegetation; BV, low-to-moderate vegetation; DD, dark desert; BD, bright desert; PS, permanent snow). Boxes delimit the two areas in which the ice/snow retrieval is applied.

Table 1
Averaged unfiltering error (bias and RMSE) as a function of the surface types and the cloud cover condition

Scene type	BIAS [%]		RMSE [%]	
	Clear	Cloudy	Clear	Cloudy
Ocean	0.04	−0.03	1.14	0.40
Dark vegetation	−0.01	−0.06	0.81	0.49
Bright vegetation	0.02	−0.10	0.99	0.55
Dark desert	0.05	−0.11	0.96	0.55
Bright desert	0.09	−0.10	0.84	0.53
Snow	0.00	0.00	0.30	0.24

where θ_s and θ_v are the solar and viewing zenith angles, respectively. ϕ is the relative azimuth angle, and finally, $\bar{R}_{SW}(\theta_s, \theta_v, \phi)$ is the CERES-TRMM BB SW ADMs anisotropic correction factor.

Because the CERES BB radiometers footprint size on the Tropical Rainfall Measuring Mission (TRMM) is about 10×10 km at the sub-satellite point, F_{SEVIRI} fluxes are not retrieved at the native SEVIRI resolution (3 km at nadir). Instead, the GERB-like SEVIRI flux, $F_{3 \times SEVIRI}$, are estimated from the mean of 3×3 SEVIRI pixel SW radiances using the appropriate CERES-TRMM ADMs based on the average scene identification (i.e., surface type and cloud properties) from the 3×3 SEVIRI pixel box. Then fluxes at the GERB footprint resolution (50 km at nadir) are derived from the 3×3 SEVIRI pixel based flux estimates.

$$F_{GERB}(i,j) = \left(\sum_x \sum_y PSF(i,j,x,y) \cdot F_{3 \times SEVIRI}(x,y) \right) \cdot C_L(i,j) \quad (8)$$

where $F_{GERB}(i,j)$ is the flux at the GERB footprint resolution $(i,j = 1, \ldots, m)$ and $F_{3 \times SEVIRI}(x,y)$ is the flux at the 3×3 SEVIRI pixel resolution $(x,y = 1, \ldots, n$ with $n > m)$. $PSF(i,j,x,y)$ is the point spread function of GERB pixel (i,j) and $C_L(i,j)$ is the correction factor (CF) at the GERB nominal spatial resolution as introduced in Eq. (1).

In a second step, the spatial resolution of the GERB fluxes is improved by use of SEVIRI high resolution information. This requires one to find CFs, $c_H(x,y)$, which applied to the high resolution flux estimates allow one to reproduce the low resolution GERB fluxes after convolution with the PSF.

$$F_{GERB}(i,j) = \sum_x \sum_y PSF(i,j,x,y) \cdot c_H(x,y) \cdot F_{3 \times SEVIRI}(x,y) \quad (9)$$

where $c_H(x,y)$ is the CF at the high (3×3 SEVIRI pixel) resolution or resolution enhancement factor.

GERB flux at the 3×3 SEVIRI pixel resolution is then given by:

$$F_{GERB/3 \times SEVIRI}(x,y) = c_H(x,y) \cdot F_{3 \times SEVIRI}(x,y) \quad (10)$$

In the following of the paper we will only consider GERB SW fluxes at the high 3×3 SEVIRI pixel resolution Eq. (10) and not the SW fluxes at the native GERB spatial resolution Eq. (8).

3. SEVIRI snow detection scheme

Use of the ratio of a SWIR channel to a VIS channel was determined by Kyle et al. (1978) and Bunting and d'Entremont (1982) to be useful for snow cover mapping, and later utilized by Dozier (1989) to map snow in the Sierra Nevada mountains. Similarly, the Moderate Resolution Imaging Spectroradiometer (MODIS) snow mapping algo-

rithm (Hall et al., 1995; Klein et al., 1998) takes advantage of the low SWIR reflectance of snow which contrast with its high VIS reflectance in its formulation. A Normalized Difference Snow Index (NDSI) is computed on a pixel-by-pixel basis from the MODIS bands 4 (centered at 0.55 µm) and 6 (centered at 1.6 µm) to determine if a pixel is snow covered ($NDSI_{MODIS} = (\rho_{0.55} - \rho_{1.6})/(\rho_{0.55} + \rho_{1.6})$, where $\rho_{0.55}$ and $\rho_{1.6}$ are the at-satellite MODIS reflectances in channels 4 and 6, respectively). The high reflectance of snow in VIS compared to the low SWIR portion of the spectrum, yields high NDSI values for snow compared to other surface materials. Due to differences in the spectral resolution of the imager instrument on board the Geostationary Operational Environmental Satellite (GOES) the major criterion used to discriminate between snow cover and other surfaces is based on the ratio of VIS-to-MIR reflectance, referred as a "Snow Index" (SI) (Romanov et al., 2000). ($SI_{GOES} = \rho_{0.6}/\rho_{3.9}$, where $\rho_{0.6}$ and $\rho_{3.9}$ are the GOES reflectances in channels 1 (centered at 0.6 µm) and 2 (centered at 3.9 µm), respectively). Because of a low reflectance of snow in MIR and high reflectance in VIS, SI enhances the difference of the spectral response of the snow from the response of the other surfaces. In general, larger VIS reflectance and SI values distinguish snow cover from snow-free land surface.

The spectral resolution of SEVIRI allows to make use of both, the VIS-to-SWIR or the VIS-to-MIR reflectance contrasts as an indicator of the snow presence. However, during daytime, MIR measurements include both the emitted thermal radiation and the reflected component of the solar radiation which therefore requires one to subtract the emitted component from the measured SEVIRI 3.9 µm radiance before to proceed. Moreover, identifying snow cover using only the NDSI or SI values results in many false signals, especially over cloud, mixed pixels, and water (e.g., Hall et al., 1995; Klein et al., 1998; Romanov et al., 2000). Therefore, the snow (and ice) identification uses SEVIRI reflectance in VIS (channel 1, centered at 0.6 µm), near-infrared (NIR) (channel 2, centered at 0.8 µm), and SWIR (channel 3, centered at 1.6 µm), and SEVIRI brightness temperatures (BT) from channels 4, 9, and 10 (centered at 3.9, 10.8, and 12.0 µm, respectively) as in Derrrien and Le Gléau (2005). The snow (and sea-ice) mapping is based on a multi-spectral threshold technique applied to each pixel located within two pre-defined areas (see Fig. 1 for the areas' definition) at each MS-8 slot during daytime on a near-real time basis as illustrated in Fig. 2. A NDSI is computed from the SEVIRI reflectances at 0.6 ($\rho_{0.6}$) and 1.6 ($\rho_{1.6}$) µm, respectively. ($NDSI_{SEVIRI} = (\rho_{0.6} - \rho_{1.6})/(\rho_{0.6} + \rho_{1.6})$).

A pixel will be mapped as snow in a non-densely forested region if (1) the NDSI is larger than a given threshold increased by a corrective factor to account for the high reflectance of snow in the forward scattering direction and (2) reflectance in SEVIRI band 2 ($\rho_{0.8}$) is larger than 20%. This excludes cloud shadows and liquid water as they can produce high values of NDSI and thus misidentified as
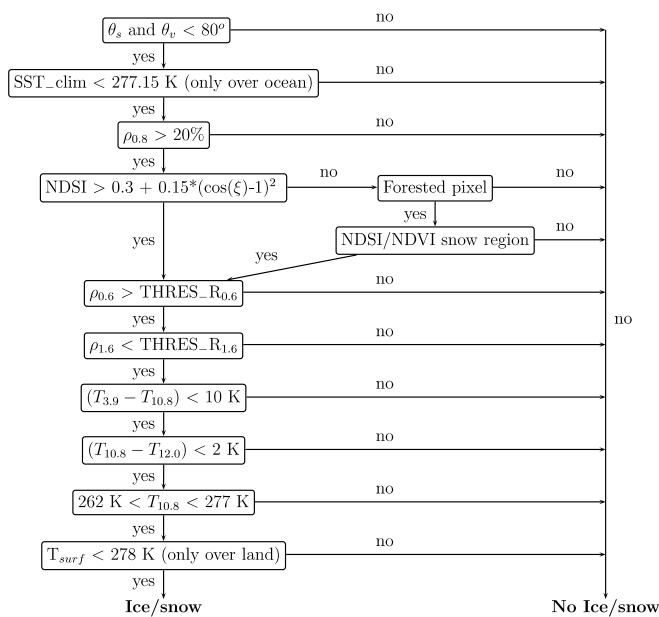
Fig. 2. Description of the ice and snow detection schemes. θ_s and θ_v are the solar and viewing zenith angles, respectively. ξ is the scattering angle $[0, \pi]$ from backward to forward direction.

snow or ice. (Liquid water may have high NDSI values as water reflects the radiation at visible bands and has strong ability of absorption in the other bands). Moreover, to prevent pixels containing very dark targets such as black spruce forests to be mapped as snow a visible threshold in the SEVIRI band 1, THRES-$R_{0.6}$, is employed. This is required because very low reflectances cause the denominator in the NDSI to be quite small, and only small increases in the visible wavelengths are required to make the NDSI value high enough to classify a pixel, erroneously, as snow (Hall et al., 2002). THRES-$R_{0.6}$ and THRES-$R_{1.6}$ (see below) are dynamical thresholds derived from theoretical radiative transfer computation of the snow surface TOA reflectances (Derrrien and Le Gléau, 2005). Note that the sea-ice detection is performed only if the SEVIRI pixel monthly climatological minimum SST value (Faugère et al., 2001) is lower than 277.15 K.

Because clouds are typically opaque in the VIS and IR spectral ranges, snow and ice retrievals are limited only to cloud-free pixels. Clouds are highly variable and may be detected by their generally high reflectance in the VIS and NIR parts of the electromagnetic spectrum (Rossow and Garder, 1993), whereas the reflectance of snow drops in the SWIR part of the spectrum. But, while the NDSI and the SEVIRI band 3 threshold, THRES-$R_{1.6}$, tests can separate snow or ice from most obscuring clouds, it does not always identify or discriminate clouds with ice tops and semi-transparent cirrus clouds as they produce a spectral signal similar to the one of snow (Miller et al., 2005). It was discovered that the BT difference $(T_{3.7} - T_{11})$ test performed in the MODIS cloud mask (with $T_{3.7}$ and T_{11} the BTs from MODIS channels centered at 3.7 and 11 μm, respectively) provided a reasonable and

improved cloud screening for the MODIS snow mapping. A similar test is adopted here by computing BT difference between the SEVIRI bands 4 and 9 centered at 3.9 and 10.8 μm, respectively ($T_{3.9} - T_{10.8}$). Additionally, the BT difference between the SEVIRI bands 9 and 10 centered at 10.8 and 12 μm, respectively, ($T_{10.8} - T_{12}$) used in the Satellite Application Facility for supporting NoWCasting and very short range forecasting (SAFNWC) cloud mask (Derrrien and Le Gléau, 2005) to detect thin cirrus cloud and cloud edges by their larger BT difference than cloud-free surfaces is also applied. To remove spurious snow cover possibly due to confusion with cloud cover, aerosol effects and snow/sand confusion on coastlines, the SEVIRI 10.8 μm thermal infrared band is used to separate snow from cloud-free region by its slightly colder $T_{10.8}$. This band is selected because it represents an atmospheric window, in which little of the emitted thermal radiation is absorbed by the atmosphere. Finally, a split-window technique using the SEVIRI thermal infrared bands 9 and 10 (Sobrino and Romaguera, 2004) is used to estimate the surface temperature, T_{surf}, over the mapped snow covered pixels. Note that similar thermal masks are also found in the MODIS and GOES snow mapping algorithms. Finally, the snow/ice detection is limited to solar zenith angle, θ_s, lower or equal to 80°. Similarly, only pixels with a viewing zenith angle, θ_v, lower or equal to 80° are considered.

Forests represent a major limitation to the mapping of snow cover as a forest canopy both obscures and shadows the snow underneath (e.g., Klein et al., 1998). Therefore, the reflectance of a forest stand with a snow cover beneath will considerably differ from that of a pure snowpack. A fundamental change that snow cover causes in the spectral response of a forest is that the VIS reflectance will often increase with respect to the NIR reflectance as snow has a much higher VIS reflectance than soil, leaves or bark. This behavior is captured in the Normalized Difference Vegetation Index (NDVI) as snow will tend to lower the NDVI (Klein et al., 1998). By contrast, much smaller changes occur in the NDSI due to the similar reflectance of snow and vegetation in the MIR wavelengths, making changes in the NDSI primarily due to reflectance changes in the VIS wavelengths, and in many cases NDSI is too low to be classified as snow. To better map snow in dense vegetation, shadows and low illumination conditions where reflectance signal is low the MODIS snow mapping algorithm use a NDSI/NDVI decision region (Klein et al., 1998) designed to capture as much of the variation in NDSI-NDVI values observed in the snow-covered forests as possible while minimizing inclusion of non-forested pixels. It was designed to include forest-covered pixels that have NDSI values lower than the current threshold yet have NDVI values lower than would be expected for snow-free conditions. The decision boundary at low NDVI values was designed to exclude to as large an extent as possible, pixels of containing a mix of snow and soil (e.g., cropland, prairie) which tend to mix along a line below this threshold. The MODIS NDSI/NDVI decision region is

used here to improve the snow mapping above moderate-to-high vegetation. NDVI is computed from the SEVIRI reflectances in band 1 and 2. ($NDVI_{SEVIRI} = (\rho_{0.8} - \rho_{0.6})/(\rho_{0.8} + \rho_{0.6})$).

Fig. 3 presents the snow-cover map for January 29, 2006 over the northern area. Because the retrieval is performed at each MS-8 slot during daytime, panel A in Fig. 3 actu-

ally shows footprints which were detected as snow covered in at least one of the available day time slots (in white) by our algorithm. Snow retrievals were compared with the daily snow cover maps produced by the Satellite Application Facility for Land Surface Analysis LSA-SAF (Land SAF) (Fig. 3B) and by the Romanov and Tarpley (2005) algorithm from SEVIRI data (Fig. 3C). Also provided is
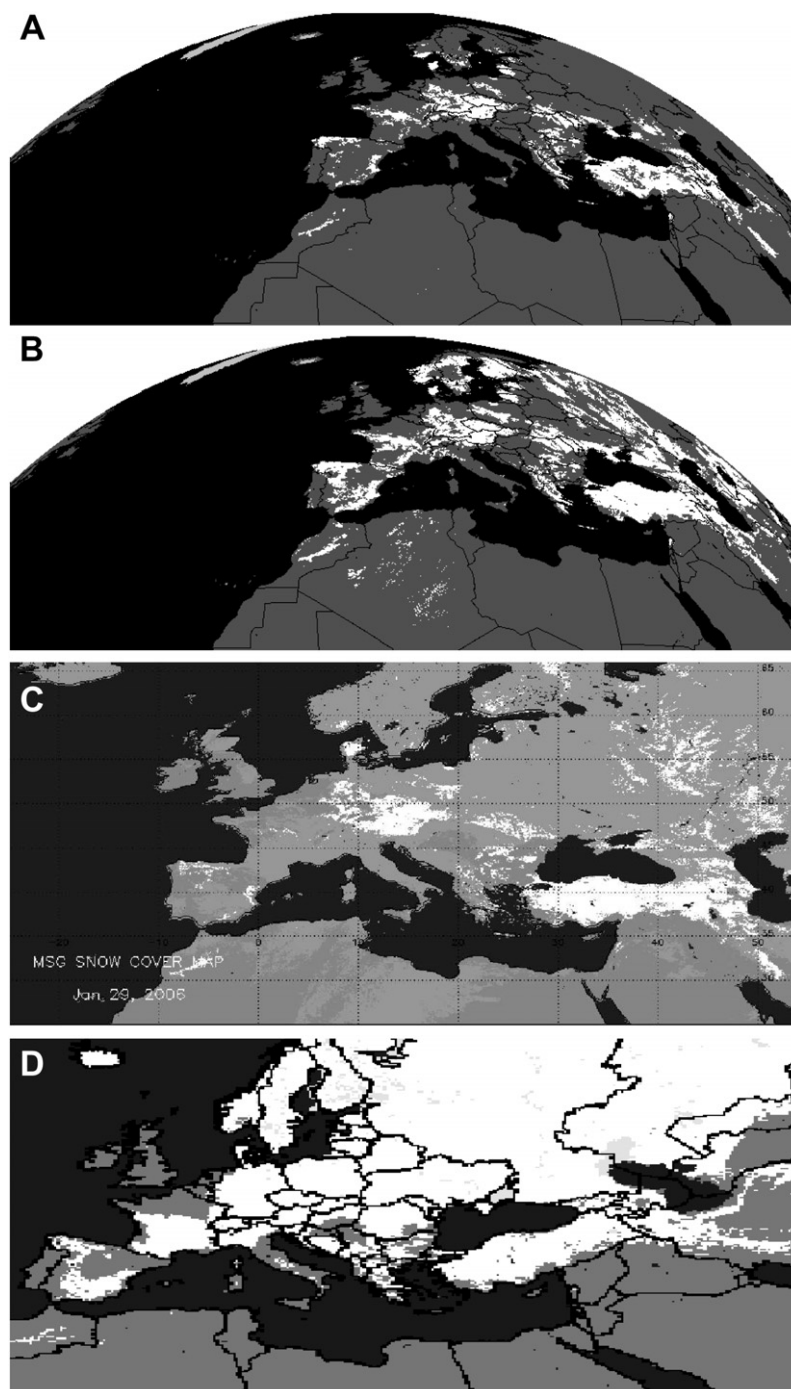

Fig. 3. Snow cover maps comparison for January 29, 2006. (A) Snow cover map over the northern area as retrieved by our algorithm from all available daytime MS-8 slots (snow covered footprints are given in white). (B) Land SAF daily snow map over the northern area computed from the SAFNWC cloud mask (Derrrien and Le Gléau, 2005). (C) Snow cover map over Europe as computed by the Romanov and Tarpley algorithm (2005) (http://www.orbit.nesdis.noaa.gov/smcddd/emb/snow/HTML/europe_snow.htm). (D) NOAA operational snow cover product (http://www.ssd.noaa.gov/PS/SNOW). Snow is given in white and sea-ice in light gray.

the snow and ice cover map from the NOAA Interactive Multisensor Snow (IMS) and Ice Mapping System (Ramsay, 1998) (Fig. 3D). The daily Land SAF snow map is derived from the cloud mask generated by the SAFNWC (Derrrien and Le Gléau, 2005) at each SEVIRI slot by applying a spatial smoothing (optional) and temporal integration of the 15 min SEVIRI slot over the 24 h satellite slots. In addition to spectral criteria the Romanov and Tarpley (2005) algorithm utilizes information on temporal variation of the scene temperature and reflectance to improve discrimination between snow and clouds in the satellite imagery. The NOAA operational daily snow product uses a combination of input data including optical and passive microwave wavelength data and surface observation. Clearly, the NOAA operational daily snow map (Fig. 3D) is not hampered by cloud cover since the passive microwave data used as input permit observation of the surface through most clouds. By contrast the three other retrievals mask out areas with any observable cloud, even thin transparent clouds, resulting in extensive areas that are masked out and not analysed by the snow algorithms (panels A–C in Fig. 3).

Comparison between the three SEVIRI-derived snow cover maps (panels A–C in Fig. 3) indicate that our snow mapping algorithm tends to underestimate snow covered pixels over Central Europe and Scandinavia (see Fig. 3A). However, adjustments performed in the multispectral thresholds used in the snow mapping algorithm to increase the number of retrieved snow covered pixels in these areas lead to generate a large number of false snow signals over the Sahara. Such an erroneous snow detection over some Saharan pixels can be observed in the Land SAF snow map in Fig. 3B. Therefore, it was preferred to have undetected snowed pixels in some conditions and keep a high degree of confidence that the mapped snow pixels are actually covered by snow.

4. Snow and sea-ice angular distribution models

Because both GERB and SEVIRI sample only a small angular portion of the total energy reflected at TOA, this angular measurement must be converted to a hemispherical quantity. If the reflections from the surface were isotropic, a single measurement would be representative of all angles. However, like most Earth surfaces, snow and ice are non-Lambertian reflector. In fact, snow is strongly forward scattering. Empirical snow and sea-ice ADMs derived from CERES Terra data (Kato and Loeb, 2005) were considered
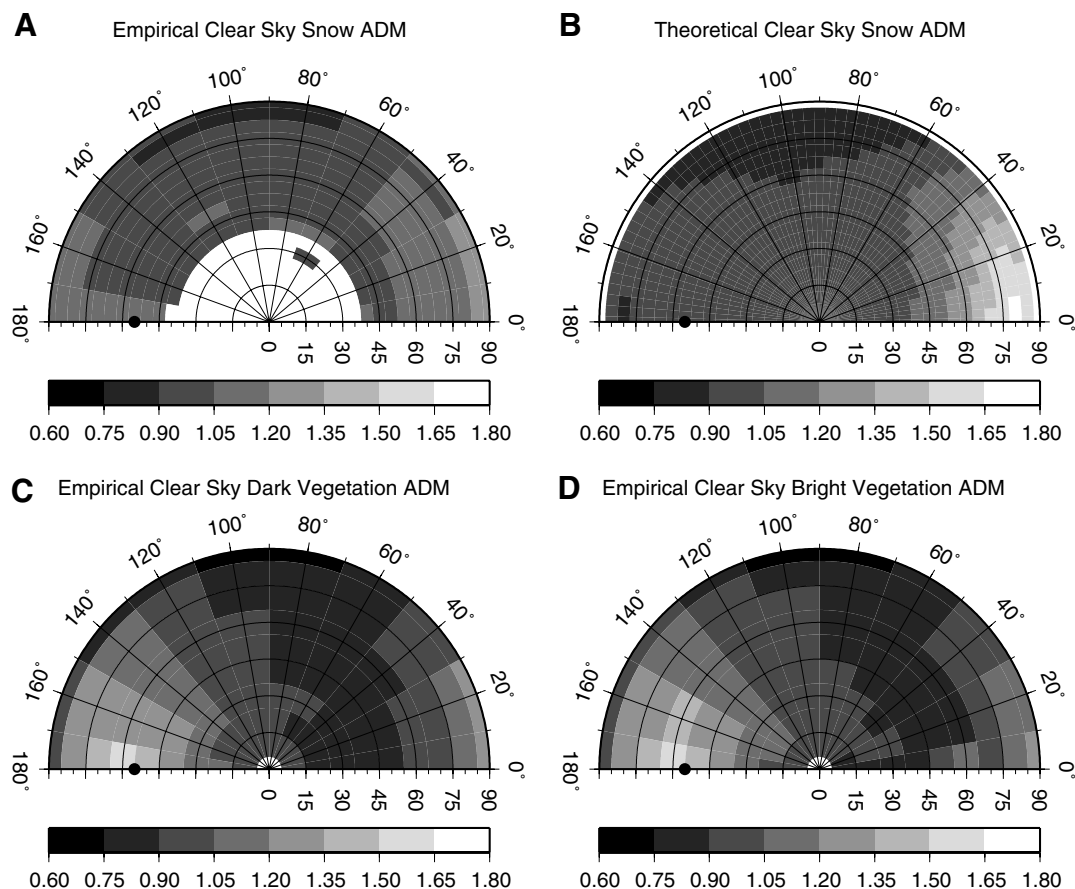

Fig. 4. Polar plots for the anisotropic correction factor of various ADM scene type: (A) empirical clear sky snow ADM from Kato and Loeb (2005), (B) theoretical clear sky snow ADM from Loeb et al. (2003), (C) and (D) empirical clear sky dark and bright vegetation ADMs from Loeb et al. (2003), respectively. Radii represent the solar zenith angles and polar angles represent the relative azimuth angles. The viewing zenith angle is 55°. Note that the central part of the panel A (central white area) has no data.

to correctly account for anisotropic scattering effects in the radiance to flux conversion Eq. (7). Permanent snow ADMs depend on cloud fraction, cloud optical depth, and snow brightness. Fresh snow and sea-ice ADMs depend on snow and sea-ice fraction, cloud fraction, cloud optical depth, and snow and ice brightness. These classifications lead to 10 scene types for permanent snow and 25 scene types for fresh snow and sea-ice in the Kato and
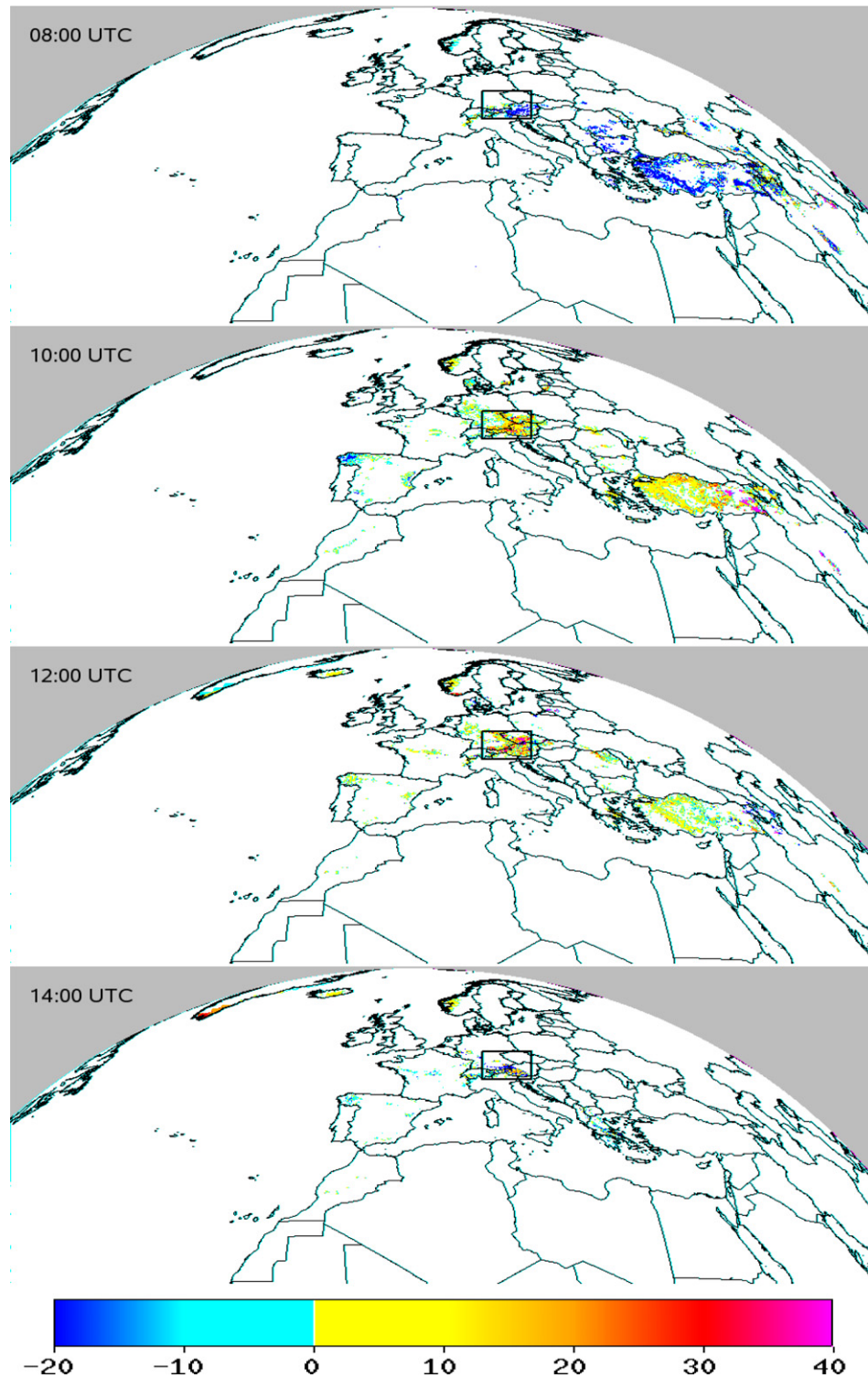

Fig. 5. Instantaneous GERB SW flux differences (in W m^{-2}) between SW fluxes computed with and without using snow (sea-ice) ADMs over the northern area. The Kato and Loeb (2005) empirical snow and sea-ice ADMs have been used for the snow (ice) computations. The differences are for January 29, 2006 at 08:00, 10:00, 12:00, and 14:00 UTC, respectively. The box centered on Austria defines the area for the flux averaging in Figs. 6 and 7.

Loeb's ADMs. Because it was not possible to retrieve snow and/or ice brightness from SEVIRI data on a near-real time basis, bright and dark ADMs were averaged reducing therefore the number of scene types to 7 for permanent snow and to 22 for fresh snow and sea-ice, respectively.

Because the Kato and Loeb (2005) empirical snow ADMs are not stratified according to the land surface type (in the snow free as in the snowed fraction of the footprints), SW fluxes were also evaluated using anisotropic correction factors (ACFs) resulting from a combination of clear sky snow ADM and bright or dark vegetation ADMs, $R_{\text{mix}}(\theta_s, \theta_v, \phi)$, to investigate if accounting for the vegetated surface type could markedly impact on the GERB SW flux-

es estimations. According to Bertrand et al. (2005) mixed scene type ACFs can be computed as follows:

$$R_{\text{mix}}(\theta_s, \theta_v, \phi) = \frac{f_1 \bar{R}_1(\theta_s, \theta_v, \phi)\bar{A}_1(\theta_s) + f_2 \bar{R}_2(\theta_s, \theta_v, \phi)\bar{A}_2(\theta_s)}{f_1 \bar{A}_1(\theta_s) + f_2 \bar{A}_2(\theta_s)}$$

(11)

where f_1 and f_2 are the snowed and snow-free fractions of the mixed footprint ($f_2 = 1 - f_1$), respectively. $\bar{R}_1(\theta_s, \theta_v, \phi)$ and $\bar{A}_1(\theta_s)$ are the clear sky snow ADM ACF and albedo, respectively. $\bar{R}_2(\theta_s, \theta_v, \phi)$ and $\bar{A}_2(\theta_s)$ are the dark or bright vegetation CERES-TRMM BB SW ADMs (Loeb et al., 2003) ACF and albedo, respectively. Two different clear
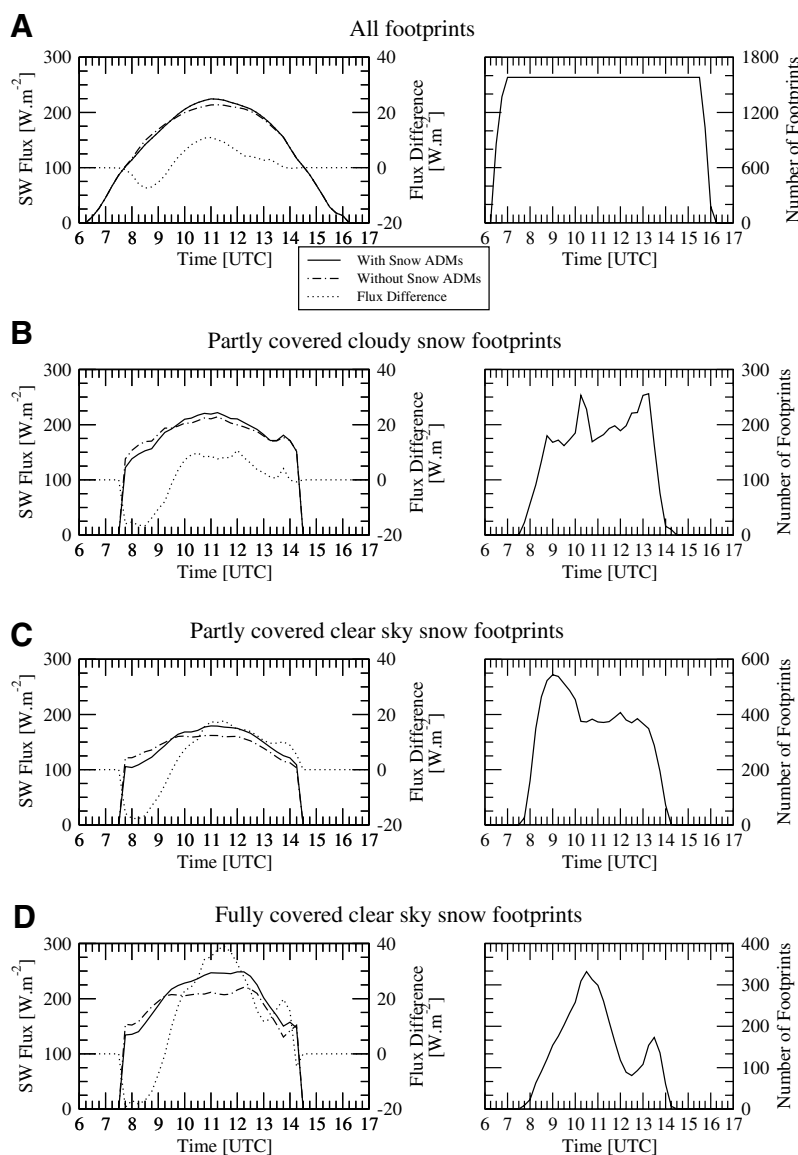

Fig. 6. Diurnal evolution from sunrise to sunset of the area averaged (see Fig. 5 for the area definition) instantaneous GERB SW fluxes computed with and without using snow ADMs (the solid and dot-dashed lines, respectively) on January 29, 2006. The Kato and Loeb (2005) empirical fresh snow ADMs have be used for the snow computations. The dotted lines give the SW flux differences between the two computations. Panel A is for all footprints found in the area regardless of the footprints scene types, panel B is for partly covered by snow cloudy footprints, panel C is for partly covered by snow clear sky footprints, and finally, panel D is for the fully covered by snow clear sky footprints.

sky snow ADMs have been considered for these additional computations, (1) the Kato and Loeb (2005) empirical clear sky fresh snow ADM and (2) a theoretical snow ADM based on 12-stream DISORT (Stamnes et al., 1998) model calculations from Loeb et al. (2003). Major differences between the empirical and theoretical snow ADMs showed in Fig. 4 (see panels A and B, respectively) are due to the influence of vegetation as the Kato and Loeb ADMs are built from directional radiance measurements made over a variety of land surface types covered by snow while the theoretical snow ADM is rather representative of the anisotropy of the radiation field over a pure snowpack which undoubtedly differ from that over a forest stand with a snow cover beneath as an example. Note that the CERES-TRMM ADM ACFs for dark and bright vegetations are given in Fig. 4 (panels C and D, respectively) for illustration.

5. Results

Fig. 5 displays instantaneous GERB SW flux differences between SW fluxes computed with and without using snow and sea-ice ADMs when performing the radiance-to-flux conversion over the mapped snow/ice footprints. The differences are for fluxes calculated with the Kato and Loeb (2005) empirical sea-ice and snow ADMs and are given for the 08:00, 10:00, 12:00, and 14:00 UTC MS-8 slots on January 29, 2006, over the northern area. Panels in this figure well indicate that the magnitude as well as the sign of the flux differences are dependent on the solar and viewing

geometry angles. This is further illustrated in Fig. 6 which presents the diurnal evolution of the area averaged instantaneous GERB SW fluxes computed with and without using the Kato and Loeb fresh snow ADMs (solid vs. dot-dashed lines, respectively) and their differences (dotted lines) when performing the angular conversion over snowed footprints. The selected area is defined by the box centered on Austria as shown in each of the Fig. 5 panels. As we see, using the Kato and Loeb fresh snow ADMs lead to first decrease the magnitude of the reflected SW flux at TOA in the vicinity of the sunset and then increase the amount of the reflected SW fux at TOA whatever the snowed scene type may be (see panels B–D in Fig. 5). While the magnitude of the flux decrease appears quite similar between the different scene types (panels B–D) with a maximum SW flux decrease of about 18 $W m^{-2}$, the largest SW flux increase occurs over the clear sky footprints fully covered by snow (panel D) and can reach up to 40 $W m^{-2}$.

Fig. 7 presents the diurnal evolution for January 29, 2006 of the area averaged (see Fig. 5 for the area definition) instantaneous GERB SW flux differences between fluxes computed with ACFs calculated according to Eq. (11) using the theoretical clear sky snow ADM or the empirical clear sky fresh snow ADM and fluxes computed with the Kato and Loeb fresh snow ADMs ACFs (black and gray lines, respectively) over the same snowed footprints as in Fig. 6. It clearly appears from this figure that the reduction in the magnitude of the GERB SW fluxes from about 7:30 to 9:30 AM reported in Fig. 6 is inherent to the use of the Kato and Loeb fresh snow ADMs as such a flux decrease
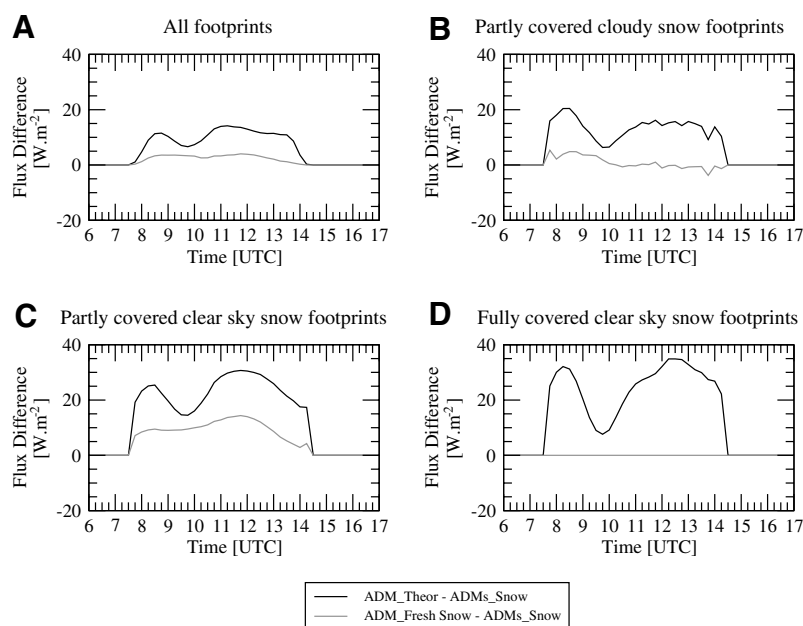

Fig. 7. Diurnal evolution from sunrise to sunset of the area averaged (see Fig. 5 for the area definition) instantaneous GERB SW flux differences between fluxes computed with mixed ACFs calculated according to Eq. (11) using the Loeb et al. (2003) theoretical clear sky snow ADM (ADM_theor) or the Kato and Loeb (2005) empirical clear sky fresh snow ADM (ADM_Fresh Snow) and fluxes calculated using ACFs from the Kato and Loeb (2005) empirical snow ADMs (ADMs_snow) (black and gray lines, respectively). The results are for January, 29, 2006. Panel A is for all footprints found in the area regardless of the footprints scene types, panel B is for partly covered by snow cloudy footprints, panel C is for partly covered by snow clear sky footprints, and finally, panel D is for the fully covered by snow clear sky footprints.

does not occur when using the theoretical snow ADM in the radiance to flux conversion whatever the snowed scene types may be (see the black lines in Fig. 7). More than compensating for the flux reduction the use of the theoretical clear sky snow ADM actually leads to a general increase in the reflected GERB SW flux at TOA from sunrise to sunset with the magnitude of the flux increase varying according to the solar and satellite viewing angles and the snowed scene types. While of reduced magnitude in regard to the flux change reported above when using the theoretical snow ADM, an increase in the instantaneous reflected SW flux (up to about 14 $W m^{-2}$) can also be identified over the clear sky footprints partly covered by snow (gray line in panel C) when using the empirical clear sky fresh snow ADM to calculate the mixed ACF according to Eq. (11). By contrast, the modifications in the instantaneous SW flux values introduced by the mixed ACFs in the SW flux computation over partly cloudy snowed footprints are quite negligible (gray line in panel B).

6. Conclusions

A snow (and sea-ice) detection scheme has been developed in order to improve the scene identification and thus the spectral and angular conversions in the near-real time processing of the GERB data at RMIB over ice/snow covered footprints. Previous versions of the algorithm did not take care of the presence of sea-ice and fresh snow covered areas within the MS-8 FOV and permanent snow was assimilated to bright desert surface when performing the radiance-to-flux conversion. While the snow and sea-ice mapping is limited by cloud cover to clear SEVIRI pixels, our results indicate that changes in the instantaneous GERB SW flux resulting from the use of empirical snow ADMs when performing the radiance to flux conversion over footprints covered by snow can be as large as 40 $W m^{-2}$. Additional calculations using pre-computed theoretical snow ADM tend to show that the magnitude of the change could even be larger over some footprints if the snow ADMs were stratified according to the land surface type in addition to the snow fraction, snow brightness, cloud fraction, and cloud optical depth as the anisotropy of the radiation field over a pure snowpack can largely differ from that over a forest stand with a snow cover beneath. Finally, our results indicate that it could also be valuable to extend the ADM land surface type stratication to the snow-free fraction in case of footprints partly covered by snow at least in clear sky condition. In the meantime the empirical snow and sea-ice ADMs derived from CERES Terra data by Kato and Loeb (2005) will be use to account for anisotropic scattering effects in the radiance to flux conversion over snow and ice covered footprints.

Acknowledgements

References

Belward, A.S. The IGBP-DIS global 1 km land cover data set (DISCover)-Proposal and implementation plans. IGBP-DIS Woring Paper No. 1 3. International Geosphere-Biosphere Programme Data and Information Services, Toulouse, France, 1996.

Bertrand, C., Clerbaux, N., Ipe, A., Dewitte, S., Gonzalez, L. Angular distribution models, anisotropic correction factors, and mixed clear-scene types: a sensitivity study. IEEE Transactions on Geoscience and Remote Sensing 43, 92–102, 2005.

Bunting, J.T., d'Entremont, R.P. Improved cloud detection utilizing defense meteorological satellite program near infrared measurements. Air Force Geophysics Laboratory Hanscom AFB, MA, AFGL-TR-82-0027, Environmental Research Paper No. 765, p. 91, 1982.

Clerbaux, N., Bertrand, C., Caprion, D., De Paepe, B., Dewitte, S., Gonzalez, L., Ipe, A. Norrowband-to-broadband conversions for SEVIRI, in: P.46 Proceedings of the 2005 Eumetsat Meteorological Satellite Conference, pp. 351–357, 2005.

Clerbaux, N., Dewitte, S., Bertrand, C., Caprion, D., De Paepe, B., Gonzalez, L., Ipe, A., Russell, J. Unfiltering of the Geostationary Earth radiation budget (GERB) data. Part I: Shortwave Radiation. Journal of Atmospheric and Oceanic Technology, 2007 (submitted for publication).

Cox, C., Munk, W. Measurements of the roughness of the sea surface from photographs of the Sun's glitter. Journal of the Optical Society of America 44, 838–850, 1954.

Derrrien, M., Le Gléau, H. MSG/SEVIRI cloud mask and type from SAFNWC. International Journal of remote Sensing 26 (21), 4707–4732, 2005.

Dirmhirn, I., Eaton, F.D. Some characteristics of the albedo of snow. Journal of Applied Meteorology 14, 375–379, 1975.

Dozier, J. Spectral signature of alpine snow cover from the Landsat Thematic Mapper. Remote Sensing of Environment 28, 9–22, 1989.

Faugère, Y., Le Borgne, P., Roquet, H. Réalisation d'une climatologie mondiale de la température de la surface de la mer à échelle fine. La Météorologie 35, 24–35, 2001 (in French).

Foster, J.L., Chang, A.T.C. Snow cover, in: Gurney, R.L., Parkinson, C.L., Foster, J.L. (Eds.), Atlas of Satellite Observations Related to Global Change. Cambridge University Press, Cambridge, pp. 361–370, 1993.

Gesell, G. An algorithm for snow and ice detection using AVHRR data: an extension to the APOLLO software package. International Journal of Remote Sensing 10, 897–905, 1989.

Hall, D.K., Riggs, G.A., Salomonson, V.V. Development of methods for mapping global snow cover using moderate resolution imaging spectroradiometer data. Remote Sensing of Environment 54, 127–140, 1995.

Hall, D.K., Riggs, G.A., Salomonson, V.V., Di Giromamo, N., Bayr, K.J. MODIS snow-cover products. Remote Sensing of Environment 83, 181–194, 2002.

Harries, J.E., Russell, J.E., Hanafin, J.A., Brindley, H., Futyan, J., Rufus, J., Kellock, S., Matthews, G., Wrigley, R., Last, A., Mueller, J., Mossavati, R., Ashmall, J., Sawyer, E., Parker, D., Caldwell, M., Allan, P.M., Smith, A., Bates, M.J., Coan, B., Stewart, B.C., Lepine, D.R., Cornwall, L.A., Corney, D.R., Ricketts, M.J., Drummond, D., Smart, D., Cutler, R., Dewitte, S., Clerbaux, N., Gonzalez, L., Ipe, A., Bertrand, C., Joukoff, A., Crommelynck, D., Nelms, N., Llewellyn-Jones, D.T., Butcher, G., Smith, G.L., Szewczyk, Z.P., Mlynczak, P.E., Slingo, A., Allen, R.P., Ringer, M. The geostationary earth

radiation budget experiment (GERB). Bulletin of the American Meteorological Society 86 (7), 945–960, 2005.

Ipe, A., Bertrand, C., Clerbaux, N., Dewitte, S., Gonzalez, L. Validation and homogenization of cloud optical depth and cloud fraction retrievals for GERB/SEVIRI scene identification using Meteosat-7 data. Atmospheric Research 72, 17–37, 2004.

Kato, S., Loeb, N.G. Top-of-atmosphere short wave broadband observed radiance and estimated irradiance over polar regions from Clouds and the Earth's Radiant Energy System (CERES) instruments on Terra. Journal of Geophysical Research 110, D07202, doi:10.1029/2004JD00530, 2005.

Key, J., Barry, R.G. Cloud cover analysis with Arctic AVHRR data. 1. Cloud detection. Journal of Geophysical Research 94, 18521–18535, 1989.

Klein, A.G., Hall, D.K., Riggs, G. Improving snow-cover mapping in forests through the use of a canopy reflectance model. Hydrological Processes 12, 1723–1744, 1998.

Kyle, H.L., Curran, R.J., Barnes, W.L., Escoe, D. A cloud physics radiometer, in: Third Conference on Atmospheric Radiation, American Meteorological society, Davis, CA, pp. 107–109, 1978.

Loeb, N., Smith, N.M., Kato, S., Miller, W.F., Gupta, S.K., Minnis, P., Wielicki, B.A. Angular distribution models for top-of-atmosphere radiative flux estimation from the Clouds and the Earth's Radiant Energy System instrument on the Tropical Rainfall Measuring Mission Satellite. Part I: Methodology. Journal of Applied Meteorology 42, 240–265, 2003.

Miller, S.D., Lee, T.F., Fennimore, R.L. Satellite-based imagery techniques for daytime cloud/snow delineation from MODIS. Journal of Applied Meteorology 44, 987–997, 2005.

Nolin, A.W., Liang, S. Progress in bidirectional reflectance modeling and applications for surface particulate media: Snow and soils. Remote Sensing Reviews 18, 307–342, 2000.

Ramsay, B. The interactive multisensor snow and ice mapping system. Hydrological Processes 12, 1537–1546, 1998.

Ricchiazzi, P., Yang, S., Gautier, C., Sowle, D. SBDART: A research and teaching software tool for plane-parallel radiative transfer in the earth's atmosphere. Bulletin of the American Meteorological Society 79, 2101–2114, 1998.

Romanov, P., Tarpley, D. Monitoring snow cover over Europe with meteosat SEVIRI, in: Proceedings of the 2005 Eumetsat Meteorological satellite Conference P.46, pp. 282–287, 2005.

Romanov, P., Gutman, G., Csiszar, I. Automated monitoring of snow cover over North America with multispectral satellite data. Journal of Applied Meteorology 39, 1866–1880, 2000.

Rossow, W.B., Garder, L.C. Validation of ISCCP cloud detections. Journal of Climate 6, 2370–2393, 1993.

Schmetz, J., Pili, P., Tjemkes, S., Just, D., Kerkmann, J., Rota, S., Ratier, A. An introduction to Meteosat Second Generation (MSG). Bulletin of the American Meteorological Society 83, 977–992, 2002.

Sobrino, J.A., Romaguera, M. Land surface temperature retrieval from MSG1-SEVIRI data. Remote Sensing of Environment 92, 247–254, 2004.

Stamnes, K., Tsay, S.-C., Wiscombe, W., Jayaweera, K. Numerically stable algorithm for discrete-ordinate-method radiative transfer in multiple scattering and emitting layered media. Appl. Opt. 24, 2502–2509, 1998.

Steffen, K. Bidirectional reflectance of snow at 500–600 nm. IAHS publication 166, 415–425, 1987.

Wielicki, B.A., Barkstrom, B.R., Harrison, E.F., Lee III, R.B., Smith, G.L., Cooper, J.E. Clouds and the Earth's Radiant Energy System (CERES): an earth observing system experiment. Bulletin of the American Meteorological Society 77, 853–868, 1996.

Wiscombe, W.J., Warren, S.G. A model for the spectral albedo of snow: 1: pure snow. Journal of the Atmospheric Sciences 37, 2712–2733, 1980.